

# A simulation environment to simulate lower-hybrid-wave-driven plasmas efficiently

journal or publication title	Computer Physics Communications
volume	230
number	September 2018
page range	38-49
year	2018-09
URL	<a href="http://hdl.handle.net/10655/00012822">http://hdl.handle.net/10655/00012822</a>

doi: 10.1016/j.cpc.2018.04.018



# A simulation environment to simulate lower-hybrid-wave-driven plasmas efficiently

Benedikt Roidl<sup>a,\*</sup>, Yasushi Todo<sup>b,c</sup>, Yuichi Takase<sup>a</sup>, Naoto Tsujii<sup>a</sup>, Akira Ejiri<sup>a</sup>, Yusuke Yoshida<sup>a</sup>, Satoru Yajima<sup>a</sup>, Takahiro Shinya<sup>d</sup>

<sup>a</sup>*The University of Tokyo, Kashiwa 277-8561, Japan*

<sup>b</sup>*National Institute for Fusion Science, Toki 509-5292, Japan*

<sup>c</sup>*The Graduate University for Advanced Studies, Toki 509-5292, Japan*

<sup>d</sup>*National Institute for Quantum and Radiological Science and Technology, Rokkasho 039-3212, Japan*

---

## Abstract

In this study a hybrid simulation environment to investigate the lower-hybrid-wave-driven tokamak plasmas is presented, and its application to the spherical tokamak TST-2 is described. These plasma are formed and driven by radio-frequency waves without the use of the central solenoid, and are characterized by low density and low magnetic field. A hybrid simulation environment which is divided into two groups, one using magneto-hydrodynamic (MHD) as well as particle-in-cell (PIC) approaches, and the second group using ray-tracing and Fokker-Planck solvers, is applied to describe the behaviour of energetic electrons, bulk plasma, wave propagation, and the wave-particle interaction. Both groups of solvers can be coupled via the energetic-particle velocity distribution function and the equilibrium conditions of magnetic field, pressure, and density profiles to obtain a self-consistent solution. First results show the impact of a self-consistent equilibrium on ray trajectories and current density profiles. Therefore, new insights in lower-hybrid-wave-driven plasmas of TST-2 can be obtained using the proposed hybrid simulation environment.

*Keywords:* Lower-hybrid wave; Current drive; MHD; Ray tracing; Fokker-Planck; Self-consistent equilibrium

---

\*Corresponding author.

*E-mail address:* roidl@fusion.k.u-toyko.ac.jp

## 1. Introduction

Spherical tokamaks (ST) possess the significant advantage of high  $\beta$  plasma capability at low magnetic field. However, until today it is not feasible to realize a compact ST reactor at low aspect ratios ( $A \leq 1.5$ ) without eliminating the central solenoid [14, 11]. During the steady-state burning phase, the plasma current could be maintained mainly by the self-driven current possibly assisted by a neutral beam current drive. To reach a sufficiently high plasma current level for burning plasma in an ST fusion reactor, there is until today no established method of effective current ramp-up without the use of the central solenoid. Note that in conventional tokamaks with aspect ratios  $A > 3$ , the plasma current was successfully ramped up by the lower-hybrid (LH) waves without using the central solenoid [20, 27]. Conventional ratio tokamaks are favorable for LH current drive since the plasma dielectric constant is lower because of the higher magnetic fields compared to ST devices [12]. In TST-2, an ST device with major radius  $R_0 = 0.36$  m, minor radius  $a = 0.23$  m, aspect ratio  $A = R_0/a \geq 1.6$ , toroidal magnetic field  $B_t \leq 0.3$  T, and plasma current  $I_p \leq 0.14$  MA [19], non-inductive plasma current start-up using LH waves has been investigated thoroughly [18, 28, 25, 15, 16]. A recently installed capacitively coupled combline (CCC) antenna [16] has a coupling efficiency of nearly 100% and can be applied at high power. Recently, plasma current ramp-up to 25 kA has been achieved injecting 74 kW of net RF power at 200 MHz. Furthermore, recent measurements showed that the bulk temperature profile is hollow, which also implies that the toroidal current density profile might also be hollow. Furthermore, in the TST-2 experiments, a small fraction of electrons at high energy are thought to carry almost the entire plasma current [24].

In the past, several numerical methods with different focus on the physics to be described have been applied to understand the TST-2 LH-driven plasmas. Initially, equilibrium reconstruction of such a plasma has been carried out using the Grad-Shafranov approach [2, 3]. Then, a full two-fluid equilibrium model [7, 6] was applied to describe a solenoid-free RF sustained ST plasma [13]. However, a certain part of the electrons being accelerated by the RF wave has higher temperatures compared to bulk electrons, i.e., there are low-density high-temperature electrons and high-density low-temperature electrons. To that end, Ishida et al. [5] developed for the simulation of collisionless ST plasmas sustained by strong RF electron heating a 3-fluid approach including MHD ordering and neglecting the gyro-

viscous cancellation. The plasma considered here consists of high-density low-temperature electrons, low-density high-temperature electrons, and high-density low-temperature ions [8]. This 3-fluid model assumed, however, that all three components have isotropic temperatures, the ion fluid is singly ionized, and that equilibrium is axisymmetric. Especially the first assumption may not describe the plasma conditions in TST-2, since studies have shown that the energetic electrons exhibit strongly anisotropic "temperatures", i.e., parallel forward temperatures are higher than perpendicular and parallel backward components along with a distribution function that is significantly different from being Maxwellian. Furthermore, the 3-fluid code uses a system of nine profile functions depending strongly on the initial choice of the shape of profiles made by the user.

Other numerical studies focused on the LH current drive mechanisms rather than the effects of resulting current profile on the ST plasma equilibrium. Previous LH current drive modeling has been largely qualitative [18, 15], because of the lack of detailed density and temperature profile information. Furthermore, some plasma parameters were tuned artificially to obtain converged simulations. A more sophisticated simulation including density and temperature profiles measured by Thomson scattering diagnostic [24] was presented recently [26], where a ray-tracing solver GENRAY [17] and a bunched-averaged Fokker-Planck solver CQL3D [4] were coupled using EFIT [9] equilibrium field for peaked distributions. It was observed that the current carrying electrons do not penetrate to the core region for a fixed magnetic field geometry such that the force balance of the plasma was not solved self-consistently. However, it was shown that for LH-driven, fully non-inductive discharges in TST-2, the correlation between the plasma current and density could be explained by using coupled GENRAY and CQL3D simulations. Still, finite orbit width, radial diffusion through collisions, and RF quasilinear diffusion were not included in the CQL3D simulation such that the quantitative analysis of RF plasma remains challenging [26].

The goal of this study is to introduce a hybrid simulation environment which is capable of simulating the conditions of an LH-driven TST-2 covering MHD fluid interacting with energetic particles, distribution function evolution via Fokker-Planck equation by RF quasilinear diffusion and collisional relaxation, and wave propagation and absorption via ray tracing. Therefore, it can handle arbitrary distribution functions, and hence, energetic electron density, pressure, and current density profiles self consistently. Since the contribu-

tion of the bulk plasma to the total pressure is about two orders of magnitude lower compared to the energetic particle contribution [24], the focus of this study is set to the significant modifications of the magnetic field configuration due to the presence of the energetic electrons.

The paper is organized as follows. First, the numerical methods are introduced in detail and the simulation procedure within the simulation environment is described. Then, the computational setup using a TST-2 LH-driven plasma configuration is given and finally, the results of the simulation environment are verified and analyzed using convergence studies and a fully coupled simulation of a typical TST-2 LH-driven plasma.

## 2. Numerical Methods

In the past, on the one hand the coupled GENRAY/CQL3D simulation has been proven useful [26, 16] to evaluate LH-wave-driven plasmas in spherical Tokamaks. On the other hand, the MHD-kinetic particle code MEGA [22, 21, 29, 23] has been successfully applied to investigate the interaction between energetic particles and the bulk plasma. For those reasons, these codes are combined and introduced in the following paragraphs whereas the focus is on MEGA since the main part of the computation applies this simulation.

### 2.1. Solvers

*MEGA*: To simulate the evolution of the energetic electrons interacting with a low-temperature bulk plasma, MEGA, a hybrid simulation code for MHD and energetic particles, is applied. In the MEGA code, the bulk plasma is described by the non-linear MHD equations and the energetic ions are simulated with the full- $f$  method instead of the  $\delta f$  particle method [1] since the simulation procedure detailed in section 2.2 targets a significant spatio-temporal modification of the self-consistent equilibrium solution. The MHD

equations with the energetic-electron effects are given by

$$\frac{\partial n_i}{\partial t} = -\nabla \cdot (n_i \vec{v}) + \nu_n \Delta (n_i - n_{eq}), \quad (1)$$

$$m_i n_i \frac{\partial \vec{v}}{\partial t} = -m_i n_i \vec{\omega} \times \vec{v} - m_i n_i \nabla \left( \frac{v^2}{2} \right) - \nabla p + (\vec{j} - \vec{j}_h) \times \vec{B} \\ - \nabla \times (\nu m_i n_i \vec{\omega}) + \frac{4}{3} \nabla (\nu m_i n_i \nabla \cdot \vec{v}), \quad (2)$$

$$\frac{\partial p}{\partial t} = -\nabla \cdot (m_i n_i \vec{v}) - (\gamma - 1) p \nabla \cdot \vec{v} + (\gamma - 1) \\ \times \left[ \nu m_i n_i \vec{\omega}^2 + \frac{4}{3} \nu m_i n_i (\nabla \cdot \vec{v})^2 + \eta \vec{j} \cdot (\vec{j} - \vec{j}_{eq}) \right] \\ + \nu_n \Delta (p - p_{eq}), \quad (3)$$

$$\vec{E} = -\vec{v} \times \vec{B} + \eta (\vec{j} - \vec{j}_{eq}), \quad (4)$$

$$\vec{j} = \frac{1}{\mu_0} \nabla \times \vec{B}, \quad (5)$$

$$\frac{\partial \vec{B}}{\partial t} = -\nabla \times \vec{E}, \quad (6)$$

$$\vec{\omega} = \nabla \times \vec{v}, \quad (7)$$

where  $n_i$  is the bulk-ion number density,  $m_i$  is the ion mass,  $\mu_0$  is the vacuum magnetic permeability,  $\gamma$  is the adiabatic constant,  $\eta$  is the resistivity,  $\nu$  and  $\nu_n$  are artificial viscosity and diffusion coefficients are chosen to maintain numerical stability. All the other quantities are conventional, whereas the subscript  $_{eq}$  represents the equilibrium variables at the beginning of the MEGA simulation. Regarding the electromagnetic field, the standard MHD formulation is applied, and using  $j_h$  in the MHD momentum equation the energetic electron contribution is included in the final coupled formulation. Note that the model accuracy does not depend on the condition that the energetic-particle density has to be significantly lower than the bulk plasma density, since electrons are used. However, in the present study the energetic electron density never exceeds 10% of the bulk-ion density. Using a fourth-order difference scheme the MHD equations are solved in space and time.

The energetic particles are described by the drift-kinetic equations [10], where

the guiding-center velocity  $u$  of the electrons is given by

$$\vec{u} = \vec{v}_{\parallel}^* + \vec{v}_E + \vec{v}_B, \quad (8)$$

$$\vec{v}_{\parallel}^* = \frac{v_{\parallel}}{B^*} \left( \vec{B} + \vartheta_{\parallel} B \nabla \times \vec{b} \right), \quad (9)$$

$$\vec{v}_B = \frac{1}{B^*} \left( -\mu \nabla B \times \vec{b} \right), \quad (10)$$

$$\vec{v}_E = \frac{1}{B} \vec{E} \times \vec{b}, \quad (11)$$

$$\vartheta_{\parallel} = \frac{m_h v_{\parallel}}{e_h B}, \quad (12)$$

$$\vec{b} = \vec{B}/B, \quad (13)$$

$$B^* = B \left( 1 + \vartheta_{\parallel} \vec{b} \cdot \nabla \times \vec{b} \right), \quad (14)$$

$$m_h v_{\parallel} \frac{dv_{\parallel}}{dt} = \vec{v}_{\parallel}^* \cdot \left( e_h \vec{E} - \mu \nabla B \right), \quad (15)$$

where  $v_{\parallel}$  is the energetic particle velocity parallel to the magnetic field,  $\mu$  is the magnetic moment,  $m_h$  is the energetic particle mass, and  $e_h = -e$  is energetic electron charge. The energetic particle current density  $j_h$  in equations 2 and 17 is given by

$$\vec{j}_h = \int e_h (\vec{v}_{\parallel}^* + \vec{v}_B) f d^3v - \nabla \times x \int \mu \vec{b} f d^3v. \quad (16)$$

with energetic particle distribution function  $f$ . Parallel velocity, magnetic curvature and gradient drifts, and magnetization current are included in the energetic particle current density. Note that the  $\vec{E} \times \vec{B}$  drift is cancelled in  $j_h$  and the momentum equation 2 due to quasi-neutrality [22]. The cylindrical coordinates  $(R, \phi, z)$  are used, where  $R$  is the major radius coordinate,  $\phi$  is the toroidal angle coordinate, and  $z$  is the vertical coordinate. Note that the finite Larmor radius was not regarded in the particle description since in the present study  $r_{Larmor}/a \ll 1$ .

For the single-sequential time-stepping scheme, which is also proposed in section 2.2, the temporal evolution of the electric field is computed via the Ampère-Maxwell law, i.e.,

$$\frac{\partial \vec{E}}{\partial t} = \epsilon_n \left( -\vec{j}_h + \int e_h \vec{v}_E f d^3v - en_i \vec{v} + \frac{1}{\mu_0} \nabla \times \vec{B} \right), \quad (17)$$

where  $\epsilon_n$  is a numerical permittivity and  $en_i\vec{v}$  is the bulk contribution. This part can be neglected in this study since the bulk contribution to the total energy is very small, i.e., the total current is approximated by the contributions of the energetic electrons.

*GENRAY and CQL3D:* In order to obtain the distribution function  $f(p_{\parallel}, \mu, R, z)$  of the energetic particles before each MEGA run, the LH-driven plasma configuration is simulated using GENRAY [17] which is coupled to CQL3D [4]. GENRAY provides as result the quasilinear diffusion coefficient evaluated from the ray trajectory and wavevector which is input for CQL3D that solves a bounce-averaged Fokker-Planck equation at zero orbit width where the electron distribution function  $f_{cql}(t, \psi, p_{\parallel}, \xi)$  as a function of magnetic flux function  $\psi$ , parallel momentum  $p_{\parallel}$ , and pitch angle  $\xi$  is evolved in time in the presence of RF fields. **Note that the results of CQL3D are computed using the coordinates  $(\psi, \theta, \phi)$ , where  $\phi$  is the toroidal coordinate and  $\psi, \theta$  are the poloidal coordinates. GENRAY and MEGA apply cylindrical coordinates  $(R, \phi, z)$ , where  $R, z$  are coordinates in the poloidal plane.**

Tsujii et al. [26] showed that the differences in the ray patterns between GENRAY and a full-wave code such as TORLH [30] has been rather small and for that reason the computationally less expensive (but from a mathematical point of view less correct) option GENRAY has been chosen to be applied in the simulation environment. In GENRAY, the toroidal and poloidal power spectrum parameters of the antenna, i.e., the index of refraction, are chosen as  $\Delta n_{\phi} = 2, n_{\phi} = 6$  and  $\Delta n_{\theta} = 1.6, n_{\theta} = 0$ . Inside the plasma, since the poloidal spectral width  $\Delta n_{\theta} < 1.6$  of the initial rays is much smaller than the poloidal index of refraction  $n_{\theta} > 70$ , ray-tracing is expected to give a reasonably accurate prediction as far as the qualitative trends are concerned. For the SOL a plasma density and temperature of  $5 \cdot 10^{16} \text{ m}^{-3}$  and 50 eV is used. In future work, due to the missing diffraction effect caused by the finite width of the poloidal spectrum and the mathematical issues it is planned to replace GENRAY by a full-wave solver.

## 2.2. A hybrid simulation environment:

The major components of the simulation environment are GENRAY, CQL3D, and MEGA. At simulation environment level, the global iteration

step  $K = [0, K_{max}]$  is applied, where  $K_{max}$  is reached at converged conditions which are further elaborated in section 4.2 . At MEGA level, the time steps  $N$  and  $n$  are used and for numerical efficiency a multi-sequential time-stepping (MSTS) scheme was applied within MEGA. The numerical procedure, presented in figure 1, can be summarized as follows:

*Step 0:* The goal of this initial step is to pass an arbitrary magnetic field configuration satisfying

$$\nabla \times \vec{B}_{EFIT} = \mu_0 \vec{j}_{EFIT}, \quad (18)$$

$$\vec{j}_{EFIT} \times \vec{B}_{EFIT} = \nabla p, \quad (19)$$

where subscript EFIT denotes to the reconstructed equilibrium values, from EFIT to GENRAY and subsequently to CQL3D at  $K = 0$ . This results in  $\vec{j}_{CQL3D} = \vec{j}^n = \vec{j}^N$  and  $\vec{B}_{EFIT} = \vec{B}^n = \vec{B}^N$  at  $n = 0$  and  $N = 0$  which is the initialization sub-time step and principal time step, respectively. Using superscripts  $N, n$  is related to MEGA and the corresponding subscript is omitted. The integrated current satisfying results of TST-2 measurement is used as a starting solution. Using a frozen target energetic particle distribution with subscript  $t$  and hence a steady current density profile  $\vec{j}_{t,h}$  that replaces  $\vec{j}_{EFIT}$  with

$$\vec{j}_{t,h}^{n,N} = \vec{j}_h^{n,N} \quad \text{at} \quad n = 0, N = 0, \quad (20)$$

where  $\vec{j}_h^{0,0}$  is computed via equation 16 using an initial, arbitrarily chosen distribution function  $f$ . In the current context the term *frozen* refers to where the distribution function of the fast electrons and hence the current density computed by equation 16 is set to  $d\vec{j}_h/dt = 0$ . In this work the fast electron distribution function from CQL3D is applied. That is,  $f_{CQL3D}(\psi_{CQL3D}, p_{\parallel}, \xi_0)$  has to be transformed to  $f_{MEGA}(p_{\parallel}, \mu, R, z)$  by mapping  $\psi_{CQL3D}$  to  $\psi_{MEGA}(R, z)$  and

$$\xi = \xi/|\xi| \sqrt{1 - B(\psi_{MEGA}(R, z), \theta) / B_{min}(\psi_{CQL3D}) (1 - \xi_0^2)},$$

where  $B_{min}(\psi_{CQL3D}) = B_{min}(\psi_{MEGA}(R, z), \theta_0)$  with poloidal angle  $\theta_0 = 0$ . The pitch angle  $\xi$  is then used to compute  $\mu = E_{kin} (1 - \xi^2) / B(R, z)$  with  $E_{kin} = 0.5 p_{\parallel}^2 / \xi^2 / m_h$ . In the following, steps A to D are computational procedures which are part of MEGA only.

*Step A:* In this first computational step within MEGA, the goal is to develop the magnetic field according to the Eulerian formulation of Faraday's law and Ampère's magnetostatic law for fixed current density profile at initial MEGA time step  $N = 1$ .

$$\vec{E}_*^n = \eta_* \left( \nabla \times \vec{B}^{n,N} - \vec{j}_{t,h}^{0,0} \right), \quad (21)$$

$$\vec{B}^{n+1,N} = -\nabla \times \vec{E}_*^n \Delta t_* + \vec{B}^{n,N}. \quad (22)$$

Since the target current density  $\vec{j}_{t,h}^{0,0}$  can be chosen arbitrarily, the magnetic field results from

$$\nabla \times \vec{B}^{n+1,N} = \mu_0 \vec{j}_{t,h}^{0,0} + \vec{R}_{res}, \quad (23)$$

where  $\vec{R}_{res}$  is a residual vector and  $\partial \vec{j}_{t,h}^{0,0} / \partial t_* = 0$ . When  $n_{max}$  is reached, the magnetic field is set to  $\vec{B}^N = \vec{B}^{n_{max},N}$ . Since there might be no solution of the magnetostatic Ampère's law in step A, a finite residual term on the right hand side is inevitable. The values for the artificial resistivity  $\eta_*$  and maximum sub-iteration step  $n_{max}$  are chosen for rapid convergence, i.e.,  $\partial \vec{R}_{res} / \partial t_* = 0$  and therewith to significantly save computational time. In this work  $\eta_* = 100\eta$ ,  $\Delta t_* = 100/\omega_{c,e}$ , where  $\omega_{c,e}$  denotes the electron gyro frequency, and  $n_{max} = 10000$  were applied. Note that quantities with the subscript  $*$  are associated to sub-iterative step  $n$  at which the energetic particle position is always kept constant.

*Step B:* The following computational step aims at the evolution of the energetic particles using the solution of step A, i.e.,  $\vec{B}^{n_{max},N}, \vec{E}^N = 0$  at  $N = 1$ , without taking into account the bulk plasma, (see step B in figure 1). This is a valid assumption since the bulk contribution to the total pressure is only about 1% and the total current density  $\vec{j} \approx \vec{j}_h$ . The magnetic field is treated using equations 6 and 4 which is changing only negligibly since the bulk plasma is not regarded in this step and the resistivity is assumed to be very low (see section 3). Step B is executed until  $N = N_{BC}$ , or  $t = t_{BC} = N_{BC} \Delta t$  with  $\Delta t = 0.5/\omega_{c,e}$

*Step C:* This step, which is similar to step A, is executed and re-iterated with step B when  $\text{mod}(N, N_{BC,step}) = 0$ , with  $N_{BC,step} = 20000$  or  $t_{BC,step} =$

$10000/\omega_{c,e}$ . The goal of step C is that for a frozen current profile, the magnetic field is evolved using equations 6 and 17, i.e.,

$$\vec{E}_*^n = \eta_* \left( \nabla \times \vec{B}^{n,N} - \vec{j}_h^{0,N} \right), \quad (24)$$

$$\vec{B}^{n+1,N} = -\nabla \times \vec{E}_*^n \Delta t_* + \vec{B}^{n,N}. \quad (25)$$

The time step  $\Delta t_*$  and numerical  $\eta_*$  are the same as in step A, which are chosen to ensure numerical stability. In this study a converging solution in step C is obtained after about  $n_{max,C} = 10000$  steps. Step B for  $0 \leq N \leq N_{BC}$  and step C at  $\text{mod}(N, N_{BC,step})$  for  $0 < n \leq n_{max,C}$  are hence executed in a multi-sequential manner until the current density distribution is converged, i.e.,  $\partial \vec{j} / \partial t = 0$ , at  $N = N_{BC} \approx 3 \cdot 10^5$ .

*Step D:* Finally, the goal of step D is to solve the full set of MHD equations coupled with the drift-kinetic equations shown in equations 1 to 7 and 8 to 15 until  $N_{max}$  is reached that corresponds to the converged state of the time averaged solution of MEGA.

The updated magnetic field configuration  $\vec{B}^{N_{max}}$  computed by MEGA along with densities and temperature at global simulation step  $K$  is fed back to GENRAY and CQL3D and the distribution function of the energetic electrons for simulation step  $K + 1$  is computed and forwarded to MEGA again (see figure 1). Note that for the simulation environment at this development stage the exchange data between MEGA and GENRAY/CQL3D is the updated equilibrium data and between GENRAY/CQL3D and MEGA only the distribution function of the fast particles computed from CQL3D serves as exchange variable.

For comparison purpose an additional numerical scheme was derived where the particle evolution, magnetic and electric field are coupled via equations 6 and 17 in a single time-stepping using Ampère-Maxwell law to describe the temporal evolution of the electric field, referred to as single-time-stepping-Ampère (STSA) approach. That is, equation 4 is neglected since the instantaneous values of the electric field using equation 17 are higher by several orders of magnitude. In case of the STSA approach steps B and C, which are functioning similar to an implicit time-stepping scheme, are not reiterated, but the simulation evolves in time at a small time step to guarantee numerical stability, i.e., rather like an explicit time-stepping scheme.

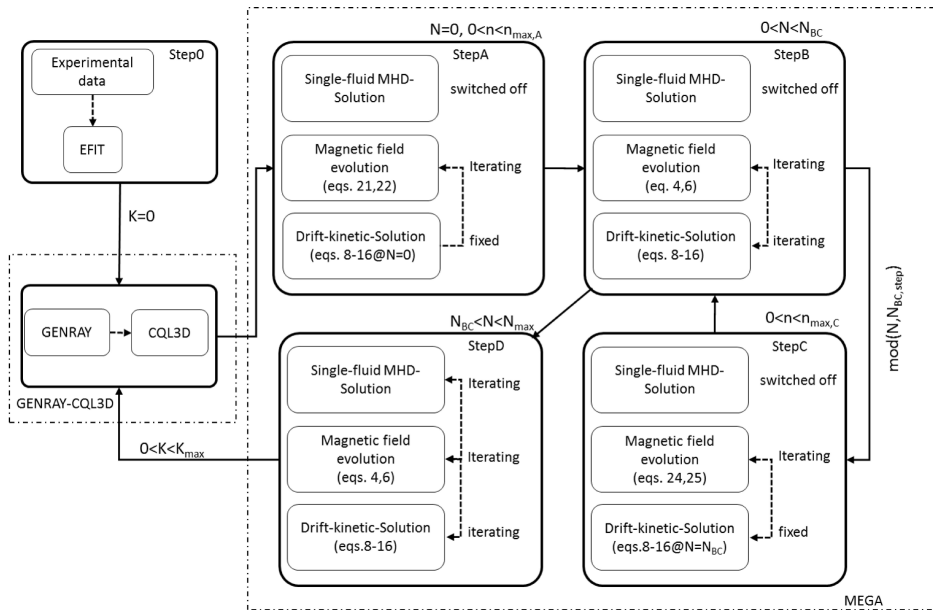


Figure 1: Procedure of the simulation environment. Left hand side shows initial solution as well as the GENRAY/CQL3D part. Right hand side shows the MEGA part including the MSTs.

When using the simulation environment including GENRAY, CQL3D, and MEGA the global simulation time step  $K_{max}$  corresponds to the converged state of the simulation environment and finally a self-consistent equilibrium is obtained.

### 3. Computational Setup

The simulation domain is defined as  $R_0 - a \leq R \leq R_0 + a$ ,  $0 \leq \phi \leq 2\pi$ , and  $-z_{lim} \leq z \leq +z_{lim}$ , where  $R_0$  is the major radius with,  $a = 0.23$  m,  $R_0 = 0.37$  m and the resulting aspect ratio  $R_0/a = 1.6$ , and  $z_{lim} = 0.4$  m. Note that the computational domain is chosen such that the boundaries represent the approximate locations of the limiters in TST-2. The number of energetic particles, i.e., energetic electrons, is set to  $4.2 \cdot 10^6$ . The viscosity and diffusivity in the simulation are set to be  $\nu = \nu_n = 10^{-6} v_A R_0 \approx 1$  m<sup>2</sup>/s and the resistivity  $\eta = 10^{-7} \mu_0 v_A R_0 \approx 1 \cdot 10^{-6} \Omega \cdot \text{m}$ , where  $v_A$  is the Alfvén velocity at magnetic axis. For grid study purposes the number of grid points of the simulations are set to (24, 16, 24), (32, 16, 32), (64, 16, 64), and (128, 16, 128) for the cylindrical coordinates  $(R, \phi, z)$ , denoted as *very coarse*, *coarse*, *fine*,

and *very fine*, respectively. The bulk plasma for the MEGA simulation is initialized using a simple fit of the experimentally measured density profile as well as constant bulk pressure as initial conditions.

The most appropriate way to simulate the particle evolution fully self-consistently in a spatio-temporally developing electro-magnetic field would be to use Ampère-Maxwell law to describe the electric field evolution which was mentioned in section 2.2. However, for reasons of numerical stability, a very small time step in the range of  $\Delta t \approx 10^{-3}/\omega_{c,e}$  has to be chosen for MEGA. This is about three magnitudes smaller than the time step associated with the MSTS scheme. Note that since in the present study the skin-depth length might be much smaller than the length scale  $l_E$  representing  $\partial \vec{E}/\partial \vec{\chi}$  with  $\chi = (R, \phi, z)$ , i.e.,  $c/\omega_p \ll l_E$  where  $\omega_p$  denotes the plasma frequency, Ampère-Maxwell law does not have to be applied to describe the temporal electric field evolution.

In this study the LH-driven plasmas in the TST-2 are investigated. These plasma configurations are usually characterized by very low poloidal beta  $\beta \leq 10^{-4}$ , low collisionality  $\nu_{ee,ei} \approx 100$  kHz, low bulk temperature  $T_{e,i} \leq 100$  eV, and low density  $n \leq 10^{18}$  m<sup>-3</sup>. In the following, the simulation parameters are based on the TST-2 experiment shot nr. 125722 at 56 ms, with  $B_0 = 0.15$  T, electron bulk density at plasma center of  $n_{e0} \approx 7 \cdot 10^{17}$  m<sup>-3</sup>, ion temperature at the magnetic axis  $T_{e0} = 10$  eV, bulk plasma beta value at the magnetic axis  $\beta_0 \approx 5 \cdot 10^{-4}$ , and the power of the outboard launch antenna of 74 kW. The low resistivity used in the numerical configuration is justified within the intended period of simulation time which is just about  $\approx 1 \cdot 10^{-5}$  s to mimic the low collisionality of the plasma, i.e.,  $1/\Lambda_D \approx 1 \cdot 10^{-5} \ll 1$ , where  $\Lambda_D$  denotes the Debye sphere. The simulation parameters for GENRAY and CQL3D, i.e., bulk temperatures and densities, SOL parameters, antenna and geometrical configurations, are the same as those presented in [26]. Note that the driven current using GENRAY and CQL3D is about one order of order of magnitude larger than the experimentally measured value [26]. In MEGA, energetic particle density will be scaled such that the experimentally measured plasma current is obtained to avoid initially significant gradients in the magnetic field configuration to ensure numerical stability.

#### 4. Results

The purpose of the section is twofold. First, the MEGA code alone is used in a time-stepping and grid convergence study to find the optimum

parameters for the following simulation coupled with GENRAY and CQL3D. Then, a TST-2 LH-driven plasma configuration is investigated using the simulation environment presented in section 2.2.

#### 4.1. Time-step and grid convergence of MEGA

The focus of this section is on the temporal and spatial convergence of the MEGA code using a generic peaked magnetic field configuration as input solution at  $K = 0$  for GENRAY and CQL3D without re-iteration of the global step, i.e.,  $K_{max} = 0$ , but otherwise using the parameters given in section 3. Since MEGA is the main contributor to the overall computational time in the simulation environment, the following grid and time-step studies are executed for MEGA only. As mentioned in the previous section the MSTS scheme is used to provide an efficient simulation within the simulation environment, i.e., the interplay between step B and step C (see figure 1). To ensure the optimum speed of MEGA along with a converged equilibrium solution the grid study and MSTS time-step study are analyzed. First, the parameters of the MSTS approach, i.e.,  $\Delta\tilde{t} = N_{BC,step}\Delta t$  with  $\Delta t = 0.5/\omega_{c,e}$  and  $N_{BC,step} = 20000$  which relates to  $t_{BC,step} = 10000/\omega_{c,e}$ , are assessed. That is, the outcome is compared to the results obtained by the STSA approach which is supposed to solve the electromagnetic field fully self-consistently with  $\Delta t \ll 1/\omega_{c,e}$  and which is outlined in the previous section. To assess the convergence the temporal evolution of the main contributors to the radial force per unit volume are analyzed. These contributors are identified to be the Lorentz force components  $j_\phi B_z$  and  $j_z B_\phi$  and the pressure force  $\partial p/\partial r$ , i.e.,

$$F_R^* = -\frac{\partial p}{\partial R} + j_\phi B_z + j_z B_\phi + R_{res,F,R}. \quad (26)$$

In figure 2 the force components over major radius are presented. It is observed that with increasing  $\Delta\tilde{t}$  the shape of the radial force components converge to the STSA case, whereas for smaller  $\Delta\tilde{t}$  the solution diverges from the STSA case. From experimental investigation, a hollow current density profile is expected which agrees with the numerical investigations if  $\Delta\tilde{t} > 5000$  for this LH-driven plasma configuration. Using the MSTS approach the particle relaxation time is very important, i.e., obtaining  $\partial\vec{j}_h/\partial t \approx 0$  before iterating again between step B and step C (see figure 1) to adjust the magnetic field. A small particle relaxation time would require the contribution of equation 17 which is not applied in the MSTS approach.

In the following the grid convergence study is analyzed. In figure 3 the radial force components over major radius  $R$  and the integrated value of  $F_R^*$  over non-dimensionalized time  $\tilde{t} = t\omega_{c,e}$  is presented. The coarse and very coarse grid configurations clearly show the same trend but differ in absolute values, whereas fine and very fine grid show results which are quantitatively very similar. The integrated radial force value converges to zero, i.e., the residual term in equation 26 goes to zero. However, the converged solution of the coarser grid configurations have a finite value which indicates that the  $R_{res,F,R}$  term, which includes e.g. the centrifugal force, contribute more significantly to the radial force balance.

Due to the verification results, all following simulations use a resolution of  $64 \times 16 \times 64$  grid points in the  $R$ ,  $\phi$ , and  $z$  direction and the number of particles was set to  $4 \cdot 10^6$ .

Regarding computational time, a single run on the simulation environment needs 24 hours on 128 cores for a  $64 \times 16 \times 64$  and  $4 \cdot 10^6$  particles, and on 512 cores  $128 \times 16 \times 128$  and  $16 \cdot 10^6$  particles, respectively, whereas GENRAY and CQL3D simulation consume about 2 hours on a single core. Using the STSA approach, the simulation time increases by one order of magnitude at least.

#### 4.2. Full TST-2 LH-driven plasma configuration

Next, the simulation environment is applied to a typical TST-2 LH-driven plasma to evaluate the global convergence of the solution environment and the plausibility of the results.

*Initial conditions at global step  $K = 0$*  First, the GENRAY and CQL3D solutions at  $K = 0$  are assessed using experimental data as initial conditions. In figure 4 the results of GENRAY and CQL3D are shown using initial conditions computed by EFIT and the experimental data from [24], i.e., at simulation step  $K = 0$ . The electron distribution function was evolved for about 40 ms with CQL3D by using the LH rays simulated by GENRAY where the rays penetrate reasonably well for the provided initial conditions. That is, in case of both GENRAY and CQL3D, 30 iteration steps have been simulated to reach steady state converged values of the plasma current. However, note that only less than one third of the input power is actually absorbed within the last closed flux surface by electron Landau damping whereas the rest is

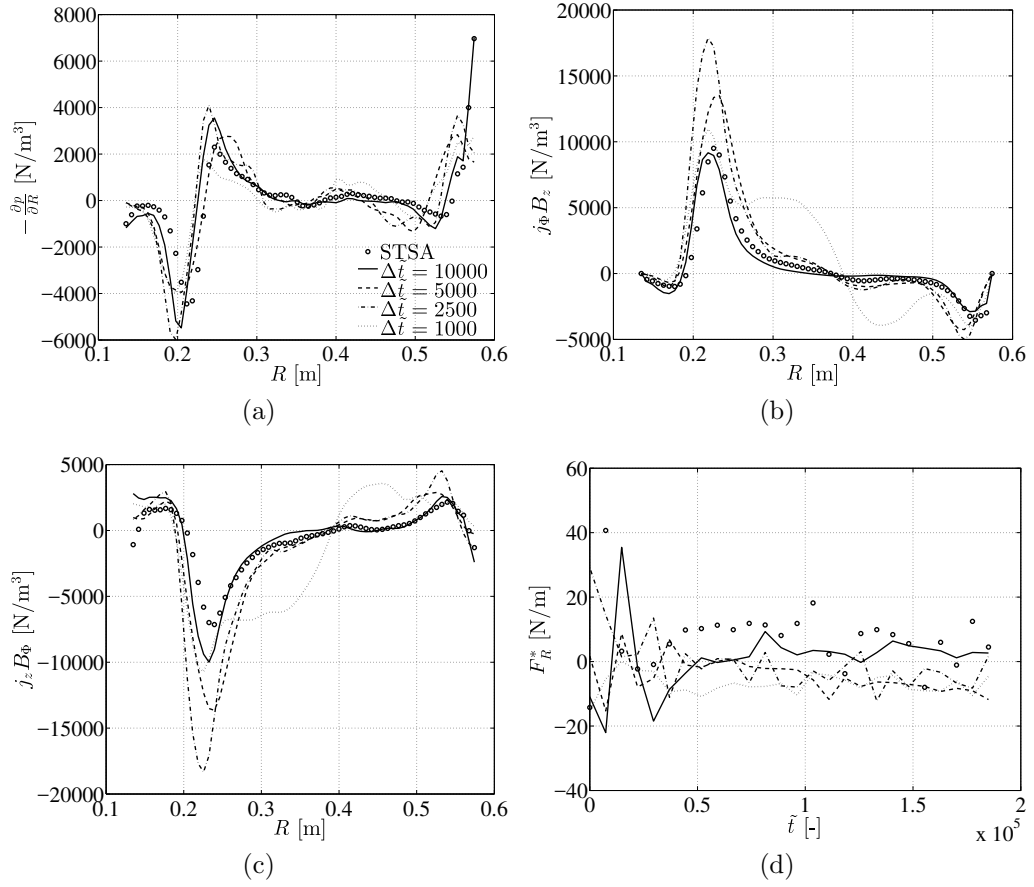


Figure 2: MEGA time-step convergence study for radial force components over major radius in (a), (b), and (c). Temporal convergence for different temporal resolutions in (d).

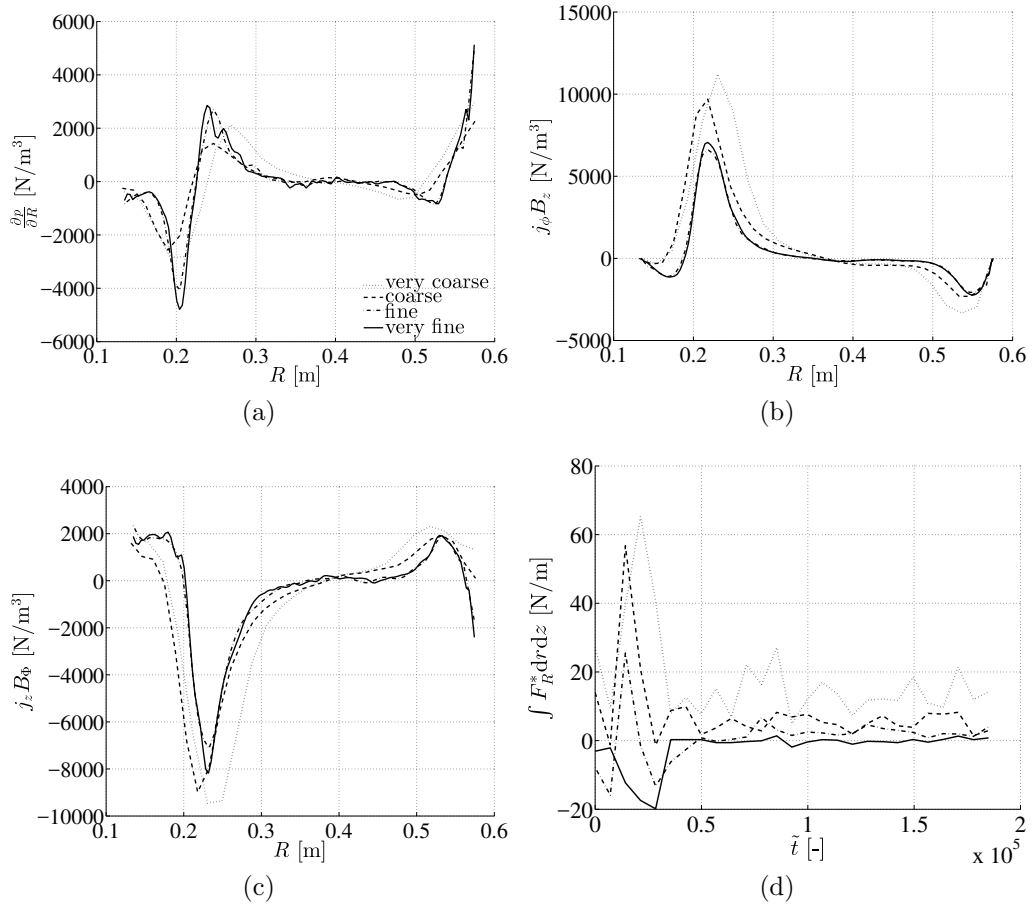


Figure 3: MEGA grid convergence study for radial force components over major radius in (a), (b), and (c). Temporal convergence for different grid resolutions in (d).

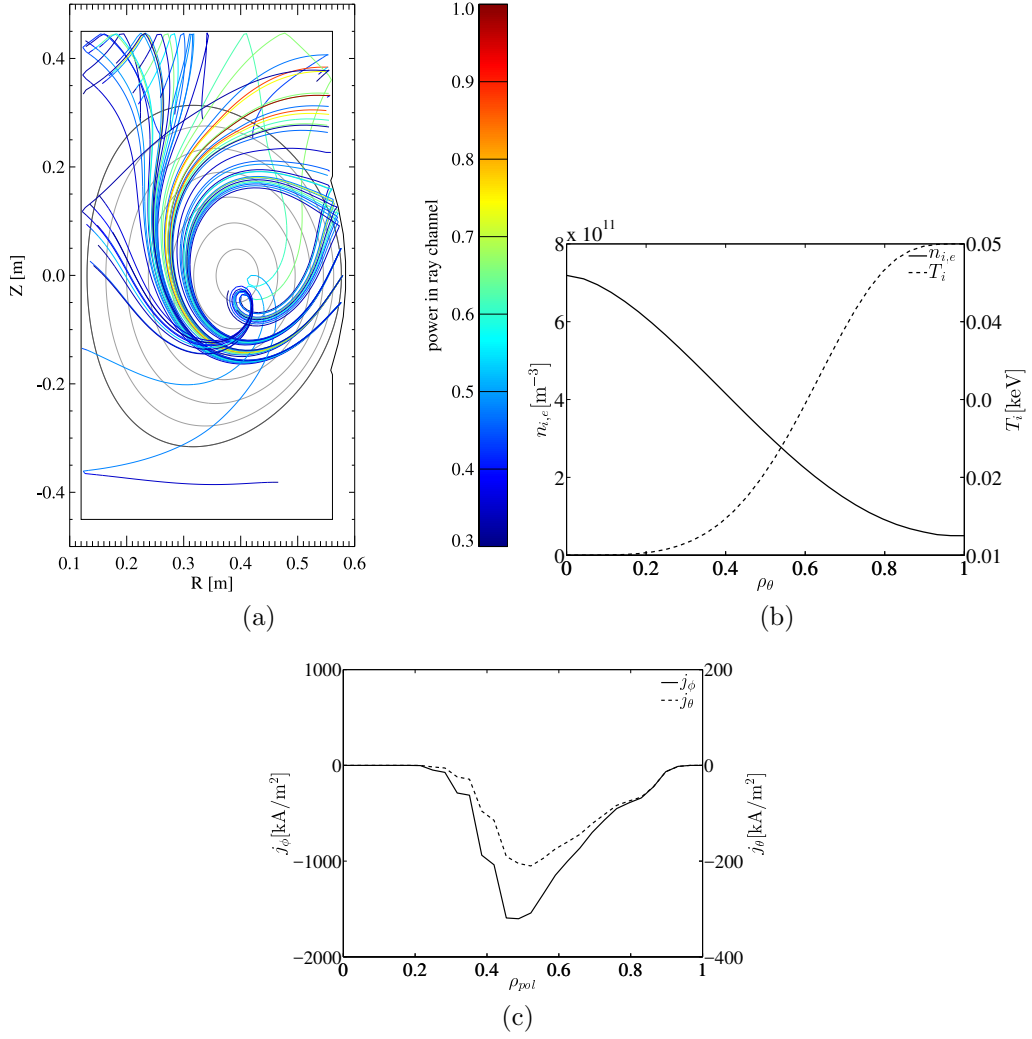


Figure 4: Initial results at  $K = 0$ : Ray trajectories computed with GENRAY, the normalized power in each channel is colored (a). Bulk density and temperature profiles (b) and toroidal and poloidal current density profiles (c) computed by CQL3D coupled with GENRAY.

absorbed in the scrape-off layer (SOL). Note that similar to previous studies [26] the background density and temperature profiles, input RF power, and magnetic field configuration are kept fixed.

This converged CQL3D solution constitutes the starting solution for MEGA. Note that the plasma current computed from CQL3D is about 150 kA (see figure 8c at  $K = 0$ ), and hence about one order of magnitude larger than that obtained by the measurements. In MEGA the density of the energetic electrons is scaled such that the initial plasma current is 25 kA and a corresponding poloidal magnetic field strength is applied. The distribution function used in MEGA as initial condition at  $K = 0$  is presented at three radial locations in figure 5. It is shown, that for the MEGA simulation nearly the entire range of the relevant part of the CQL3D distribution function of the energetic electrons is covered. However, particle velocities of  $v_{\parallel, max} \geq 1.35 \cdot 10^8$  m/s have been omitted since MEGA is not adapted to relativistic velocities and to keep  $(v_{\parallel, max}/c)^2 \leq 0.2$ . Note that the distribution function values for the perpendicular and backward parallel part are two to three orders of magnitude lower than the forward parallel part. Furthermore, at  $\rho_{pol} = r/a \approx 0.4$  the highest distribution function values are obtained in the energetic electron velocity distribution.

*Evolution and convergence of the solution for  $0 \leq K \leq K_{max}$*  The hybrid simulation environment was then iterated until a convergence of both parts of the solver, i.e., MEGA on the one hand, and GENRAY/CQL3D on the other hand is obtained.

Figure 6 shows the toroidal current evolution computed by MEGA from  $K = 0$  to  $K = 7$ . The hollow structure of the current distribution is conserved for the entire simulation. However, at  $K = 0$ , the current maxima are located closer to the magnetic axis and with progressing simulation steps the region of current maxima is pushed further towards the plasma boundary. Furthermore, due to the hollow current density profile, the flux surfaces become elongated in the vertical direction  $z$  to satisfy magnetostatic Ampère's law. Note that, since for  $K = 0$  a magnetic field configuration for a peaked current density profile was assumed by EFIT, the actual current density profile in MEGA using the distribution function of CQL3D has a rather circular shape. At e.g.  $K = 6$ , which is in this study actually  $K = K_{max} - 1$ , the current density distribution is stretched vertically due to the elongated

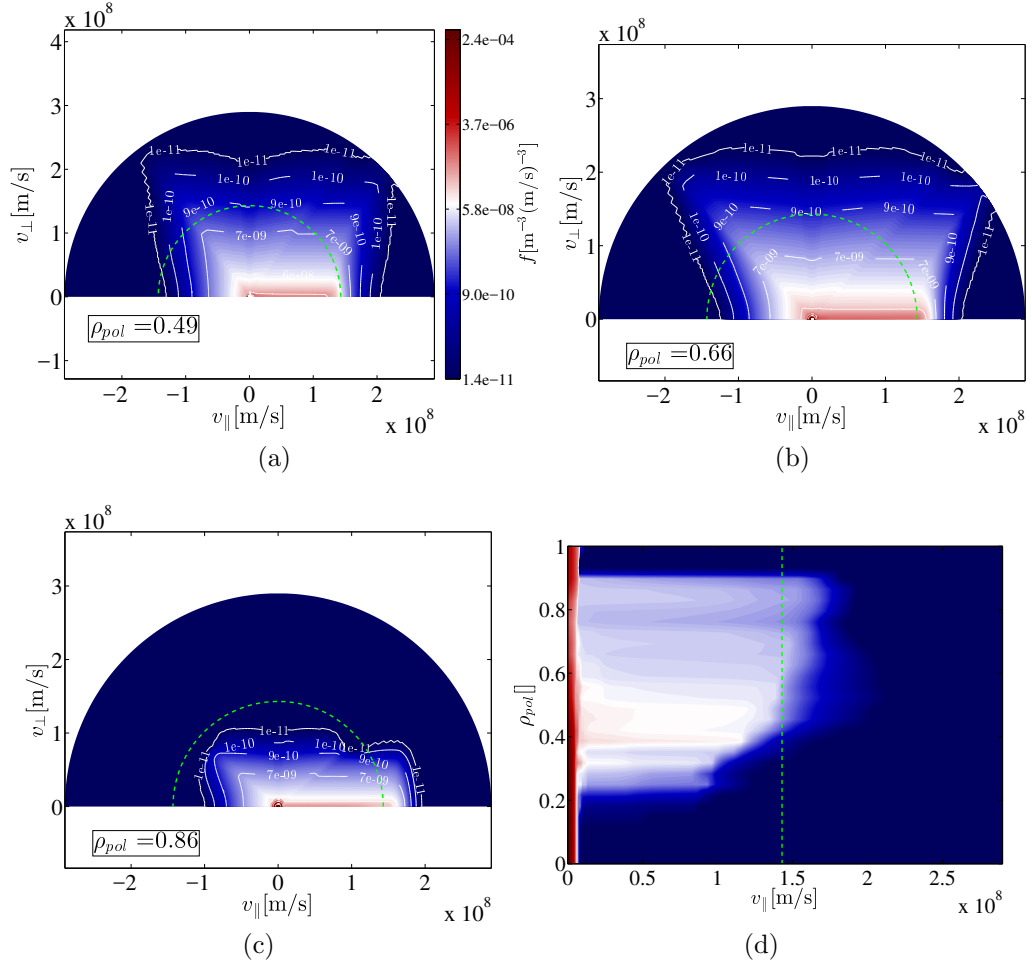


Figure 5: Distribution function as a function of parallel and perpendicular velocity at three radial locations, (a)-(c), and as function of parallel velocity and radial position at pitch angle  $\xi = 0$ , (d). Distribution function values are also contoured and labeled. The green dashed line shows maximum particle speed applied for the particle evolution in MEGA

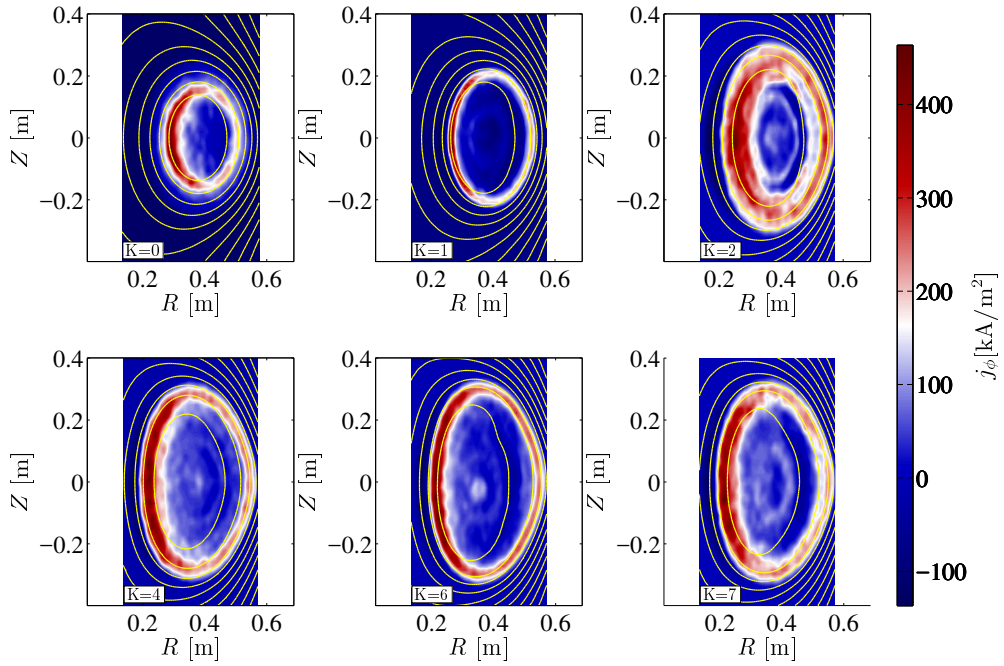


Figure 6: Global evolution of the toroidal current density shown in the poloidal plane computed by MEGA for global simulation step  $0 \leq K \leq K_{max}$ . Magnetic flux surfaces are plotted in full yellow lines.

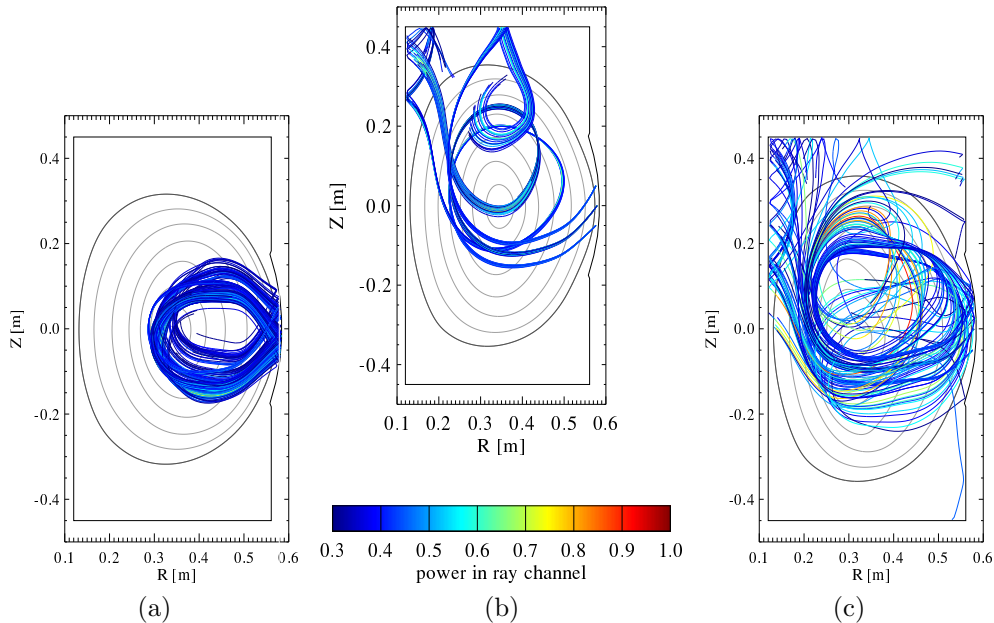


Figure 7: Global evolution of ray trajectories computed by GENRAY for global simulation steps  $K = 2$  (a),  $K = 5$  (b), and  $K = 7$  (c).

magnetic flux surfaces in vertical direction and its principal shape does not change anymore significantly for  $K_{max} - 3 < K \leq K_{max}$ . Similar to the experiments [24] a radial shift of the magnetic axis from  $R_{mag,K=0} \approx 0.395$  m to  $R_{mag,K=K_{max}} \approx 0.34$  m is observed. Note that a careful evolution of the magnetic flux configuration is necessary within each simulation step  $K$  to ensure a global convergence of the simulation environment. That is, the coefficients in equations 21 and 22 must be chosen carefully to avoid the occurrence of multiple magnetic axes which may destabilize the MHD-particle evolution in MEGA leading to unreliable results. Furthermore, since the contribution of the bulk plasma to the total pressure is about two orders of magnitude lower compared to the energetic particle contribution, the bulk density and temperature profiles do not change to that extent compared to the magnetic field for  $0 \leq K \leq K_{max}$ . That is why, the focus of this study is on the significant modifications of the magnetic field configuration due to the presence of the energetic particles.

The modified magnetic field computed in MEGA due to the evolution of

the energetic electrons and the bulk plasma at global simulation step  $K$  is fed back to GENRAY/CQL3D to obtain a new particle distribution function at  $K = K + 1$ . In figure 7 the ray trajectories at different simulation steps  $K$  are shown. Compared to the wave trajectories at  $K = 0$  shown in figure 4a, the trajectories at  $K = 2$  are already quite different since nearly all the rays are deflected more strongly towards the outboard antenna leading to multi-pass pattern with very low absorption. By progressing the simulation to  $K = 5$  and further to  $K = 7$  it is observed that the ray trajectories are also strongly deflected back to the outboard antenna after the first pass through the plasma. In case of  $K = 5$  the rays are still bundled after the first pass showing very little diffraction and a very low absorption in the inboard region of the plasma compared to the  $K = 0$  case. In case of  $K = 7$ , the magnetic field configuration is responsible to deflect the rays back to the outboard region showing a multi-pass pattern with rather randomized diffraction in the entire poloidal plane. Compared to the case for  $K = 5$ , the scattering of the rays is more pronounced, but a significant part of the absorbed LH-power still occurs in the SOL and the walls. That is, for the simulation results  $K > 2$  one major difference compared to the initial solution is that the rays only get gradually absorbed in regions near the boundary of the plasma after several passes through the plasma instead of a desired single-pass absorption which can be one reason for the degraded current drive efficiency.

By using the LH rays from GENRAY at each step  $K$  for the computation of the current driven in CQL3D a converging trend can be observed which is presented in figure 8. The radial distribution of the toroidal current density  $j_\phi$  shown in figure 8a starts at  $K = 0$  with values of about 1800 kA/m<sup>2</sup> at  $\rho_{pol} \approx 0.45$ . With progressing  $K$ , the current density is reduced and its peak shifts to  $\rho_{pol} \approx 0.65$ , which corresponds to the GENRAY computed LH ray diffraction behaviour shown in figure 7. A similar trend for the poloidal current density  $j_\theta$  is observed in figure 8a, i.e., gradually reduced current densities. Due to non-resonant collision a major part of the LH-power is absorbed in the SOL whereas in the core of the plasma Landau damping is the dominant absorption mechanism. Note that the SOL and the core absorption are comparable during  $0 \leq K \leq K_{max}$ , however, at  $K = K_{max}$  the prompt orbit losses computed by CQL3D seem to be considerably higher compared to  $K = 0$  which in turn also leads to a significantly lower plasma current.

In this study the focus of convergence was, among others, on the plasma current value obtained from CQL3D since its convergence to a steady value

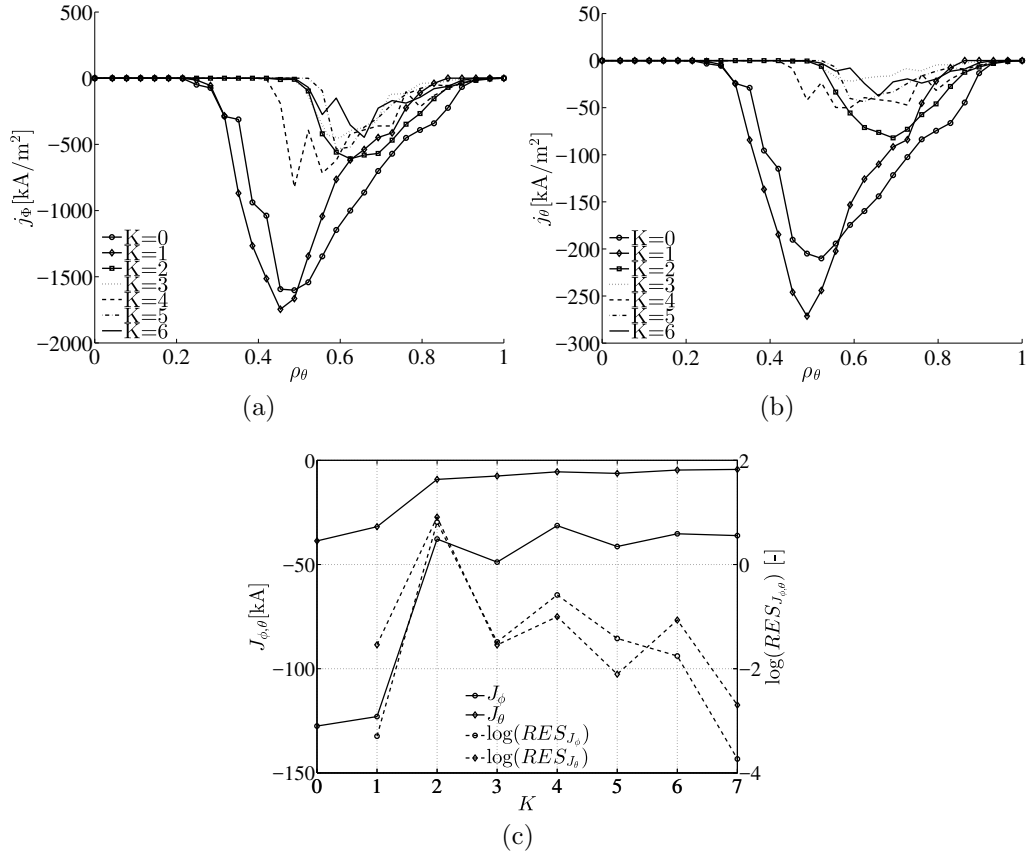


Figure 8: Global evolution of the fluxed-surface-averaged (a) toroidal and (b) poloidal current density profiles and (c) integrated current components computed by CQL3D for global simulation steps  $1 \leq K \leq K_{max}$ .

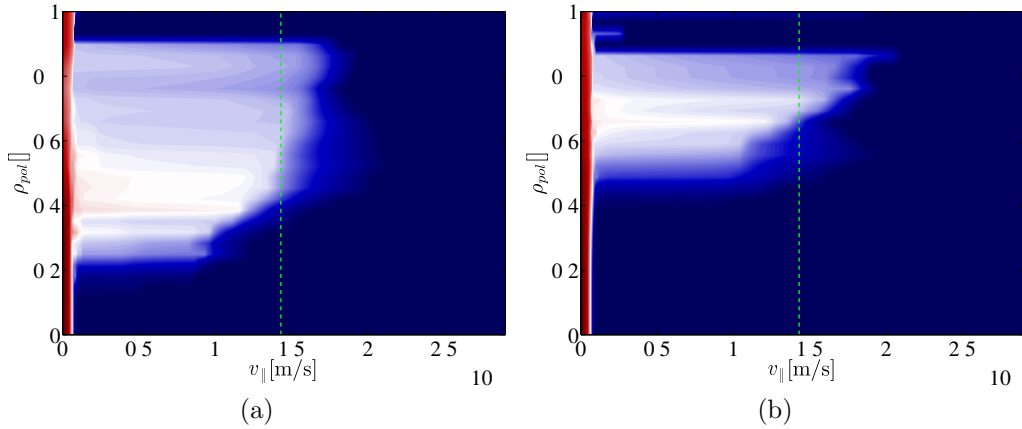


Figure 9: Distribution function as function of parallel velocity and radial position for  $\xi = 0$ . The green dashed line shows the maximum particle speed applied for the particle evolution in MEGA. (a) at  $K = 0$ , (b) at  $K = K_{max} = 7$ .

as function of  $K$  also strongly depends on the evolution of the magnetic field configuration and distribution function. The evolution of the integrated current densities over  $K$  is shown in figure 8c. For  $K \leq 1$  the plasma current has similar values as discussed in [26], i.e.,  $J_\phi \approx 140$  kA. However, after significant reduction the plasma current reaches a converged constant value for  $K \geq 3$ . The residual values of the plasma currents drop by several orders of magnitude, where the residual is computed via  $RES_{J_\phi, J_\theta} = |J_{\phi, \theta}^K - J_{\phi, \theta}^{K-1}| / |J_{\phi, \theta}^K|$ . Note that the maximum value of the plasma current at  $K = K_{max}$  is about 35 kA which is only a factor of 1.5 higher than the experimentally measured value of about 25 kA.

The radial profiles of either  $j_\phi$  nor  $j_\theta$  collapse to a single distribution but rather exhibit a substantial uncertainty in its peak value and location. This is due to the sensitivity of the ray trajectories computed by GENRAY, and although similar trends in the current density distribution are seen for  $K \geq 3$  in figure 8a, the ray trajectories and their diffraction/reflection behaviour differ visibly. However, the impact of the different radial current density distributions for  $K \geq 3$  on the integrated current is relatively small.

The resulting distribution function of the energetic electrons at pitch angle  $\xi = 0$  computed by CQL3D at  $K = K_{max}$  is presented in figure 9 and compared to the initial distribution at  $K = 0$ . As already discussed in figures 8a and 8b, the maximum driven current density is shifted outboard and its

value is reduced during the course of the simulation. These phenomena are also observed in the distribution function peak in radial direction which was significantly shifted to  $\rho_{pol} \geq 0.6$  and the energetic electron plateau ends at lower velocities compared to the solution at  $K = 0$ .

After assessing the evolution and convergence of the plasma current computed by CQL3D, the resulting distributions of the bulk plasma ion temperature and ion density as well as the evolution of the radial current density distribution computed by MEGA is discussed. In figures 10a and 10b the profile of the bulk ion density and ion temperature at  $K = K_{max}$  are presented. The agreement of the numerical results with experimental values [24] is satisfying. A more thorough analysis of the bulk plasma properties is, however, beyond the scope of this paper and will be part of future work. In figure 10c the evolution of the radial toroidal current density profile is shown. Similarly to the current density profiles shown in figure 8a, the resulting peak of the MEGA solution at  $K = 0$  at  $R = 0.3$  m roughly corresponds to  $\rho_{pol} \approx 0.4$ , also at  $K = 0$ . For the following steps  $K > 0$  the current density peak located on the inboard side is eventually converges to  $R \approx 0.21$  m which is  $\rho_{pol} \approx 0.6$ . Note that the CQL3D solution for  $K \geq 3$  being the initial solution at  $N = 0$  to MEGA is located further outboard compared to MEGA at  $N = N_{max}$  which means that the particle evolution in MEGA causes a slight inboard shift of the current density profile. Furthermore, due to the missing radial diffusion term and the zero-orbit approximation, the CQL3D solution has zero current near the plasma center whereas the MEGA solution shows a finite plasma current near the magnetic axis due to the particle evolution using drift-kinetic equations. Similar to the bulk plasma properties the detailed evolution of energetic particles is part of the future work.

The plasma current and the corresponding residual as well as the residuals of the magnetic flux function computed by MEGA are shown in figure 10d. Similar to figure 8c, the residuals of the plasma current drops by several orders of magnitude when  $K$  reaches  $K_{max}$ . Note that also the spatially averaged residual of the magnetic flux function  $RES_{\psi} = \langle |\psi^K - \psi^{K-1}| \rangle / \max(|\psi^K|)$  drops by one-to-two orders of magnitude .

Finally, for  $K \geq 4$  the solutions obtained by the simulation environment converge in terms of magnetic field configuration and current density profiles obtained by MEGA and the evolution of the plasma current computed by CQL3D. The ray trajectories computed by GENRAY are very susceptible to

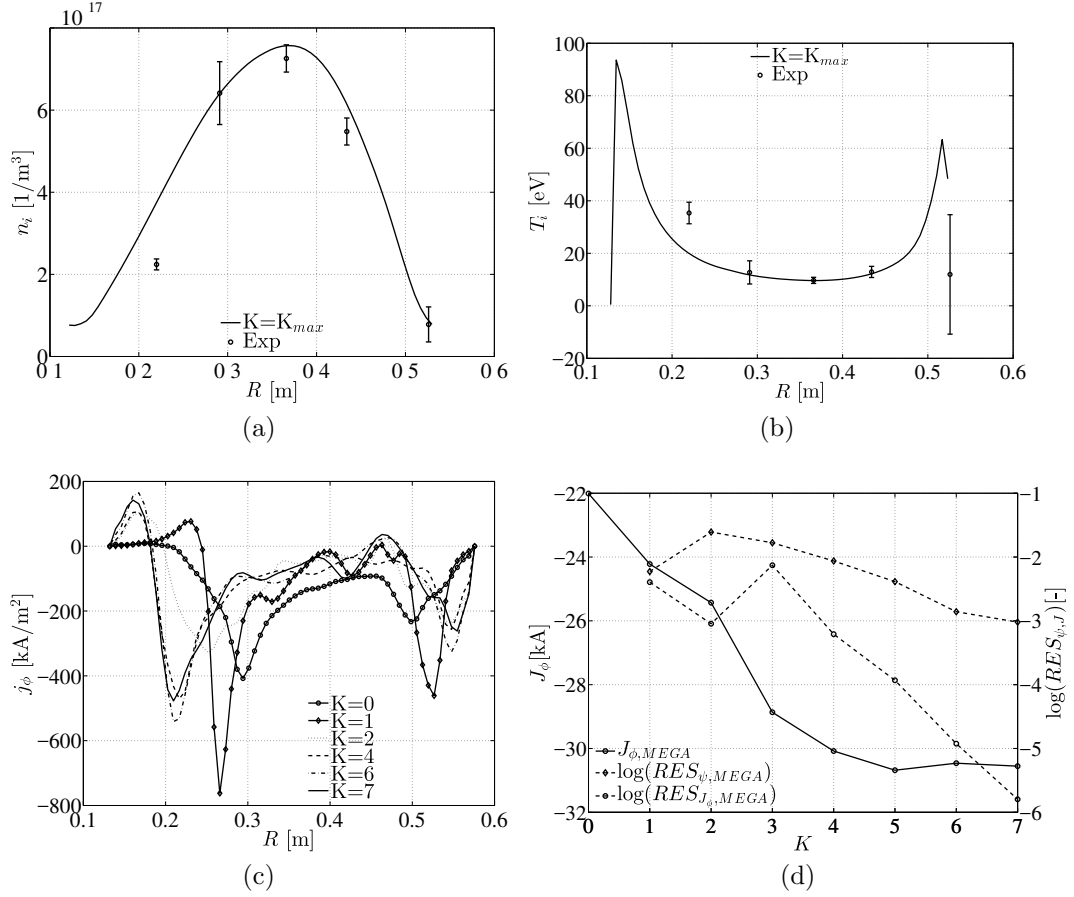


Figure 10: Radial profiles of (a) bulk ion density, (b) bulk ion temperature at  $K = K_{max}$ , toroidal current density (c), and evolution of plasma current and the residual values of plasma current and magnetic flux function (d) computed by MEGA for the global simulation step  $0 \leq K < K_{max}$

the magnetic field configuration computed by MEGA. However, for  $K \geq 3$  the impact of these changes on the subsequent CQL3D computations is not significant in terms of the integral plasma current.

## 5. Conclusions

In this study a hybrid simulation environment consisting of three different codes was presented in detail to investigate the LH-driven plasma configurations of the TST-2 spherical tokamak. The simulation environment used an MHD-PIC approach called MEGA and a coupled ray-tracing/Fokker-Planck solver GENRAY/CQL3D. MEGA is coupled to GENRAY/CQL3D in this study via the distribution function of the energetic electrons and the magnetic field configuration. The time-step and grid-convergence study was analyzed to find the optimum parameter for the MEGA code in this simulation environment regarding computational efficiency whereas simulation parameter of GENRAY and CQL3D remained unchanged compared to previous studies of the same TST-2 configuration.

The simulation environment was applied to a realistic LH-driven plasma configuration. It was shown that by iterating the solutions of MEGA and GENRAY/CQL3D, the initial plasma current computed by CQL3D decreased from about 140 kA to about 35 kA, which is close to the experimentally measured value of about 25 kA. The main reason for the decreasing plasma current is the updated equilibrium solution provided by MEGA. The updated magnetic field configurations caused a significant change in ray-trajectory topologies which led to reduced power absorption near the plasma center, but increased absorption near the plasma boundary and orbit losses. Global convergence was demonstrated by the integral plasma current evolution computed by CQL3D and the radial current density profiles computed by MEGA which were obtained after about 6 to 7 iterative cycles. A more detailed analysis regarding energetic particle orbit loss mechanisms, ray trajectories, etc. of the LH-driven plasma obtained by the simulation environment will be reported in a separate publication.

Because of the very small time step of the STSA approach, i.e.,  $\Delta t \ll 1/\omega_{c,e}$ , it would be theoretically possible in the future to introduce LH waves into the computational domain of MEGA and compute the distribution function evolution using a Fokker-Planck approach in MEGA which would replace the GENRAY/CQL3D part of the simulation environment. These recent results encourage the optimization of future antenna configuration to further

increase the efficiency of current drives using LH waves in spherical and conventional tokamaks.

## **6. Acknowledgements**

This study was supported by the DFG postdoctoral scholarship (Nr. 5145/1) and it was performed on "Plasma Simulator" (FUJITSU FX100) of NIFS with support and under auspices of the NIFS Collaborative Research (NIFS16KNXN345 and NIFS17KNST110).

## References

- [1] A. Dimits and W. W. Lee. Partially linearized algorithms in gyrokinetic particle simulation. *Journal of Computational Physics*, 107(2):309–323, 1993.
- [2] A. Ejiri, Y. Takase, H. Kasahara, T. Yamada, K. Hanada, K. Sato, H. Zushi, K. Nakamura, M. Sakamoto, H. Idei, et al. RF start-up and sustainment experiments on the TST-2@ K spherical tokamak. *Nuclear fusion*, 46(7):709, 2006.
- [3] A. Ejiri, Y. Takase, T. Oosako, T. Yamaguchi, Y. Adachi, O. Watanabe, Y. Nagashima, B. An, H. Kobayashi, H. Kurashina, et al. Non-inductive plasma current start-up by EC and RF power in the TST-2 spherical tokamak. *Nuclear Fusion*, 49(6):065010, 2009.
- [4] R. Harvey and M. McCoy. The CQL3D Fokker-Planck code. *Advances in Simulation and Modeling of Thermonuclear Plasmas*, page 498, 1992.
- [5] A. Ishida, A. Ejiri, Y. Takase, N. Tsujii, H. Togashi, Y. Yoshida, T. Shinya, and S. Tsuda. Three-fluid axisymmetric equilibrium model and application to spherical torus plasmas sustained by RF electron heating. *Plasma and Fusion Research*, 10:1403084–1403084, 2015.
- [6] A. Ishida and L. C. Steinhauer. Spherical torus equilibria reconstructed by a two-fluid, low-collisionality model. *Physics of Plasmas*, 19(10):102512, 2012.
- [7] A. Ishida, L. C. Steinhauer, and Y.-K. M. Peng. Two-fluid low-collisionality equilibrium model and application to spherical torus plasmas. *Physics of Plasmas*, 17(12):122507, 2010.
- [8] W. Jones, A. Lee, S. Gleman, and H. Doucet. Propagation of ion-acoustic waves in a two-electron-temperature plasma. *Physical Review Letters*, 35(20):1349, 1975.
- [9] L. Lao, H. S. John, R. Stambaugh, and W. Pfeiffer. Separation of  $\beta_p$  and  $i$  in tokamaks of non-circular cross-section. *Nuclear Fusion*, 25(10):1421, 1985.
- [10] R. G. Littlejohn. Variational principles of guiding centre motion. *Journal of Plasma Physics*, 29(01):111–125, 1983.

- [11] F. Najmabadi and A. Team. Spherical torus concept as power plantsthe ARIES-ST study. *Fusion Engineering and Design*, 65(2):143 – 164, 2003.
- [12] M. Ono. High harmonic fast waves in high beta plasmas. *Physics of Plasmas*, 2(11):4075–4082, 1995.
- [13] Y.-K. M. Peng, A. Ishida, Y. Takase, A. Ejiri, N. Tsujii, T. Maekawa, M. Uchida, H. Zushi, K. Hanada, and M. Hasegawa. Two-fluid equilibrium considerations of Te/Ti 1, collisionless st plasmas sustained by RF electron heating. *Plasma and Fusion Research*, 9:3403146–3403146, 2014.
- [14] Y. M. Peng and D. J. Strickler. Features of spherical torus plasmas. *Nuclear Fusion*, 26(6):769, 1986.
- [15] T. Shinya, Y. Takase, T. Wakatsuki, A. Ejiri, H. Furui, J. Hiratsuka, K. Imamura, T. Inada, H. Kakuda, H. Kasahara, et al. Non-inductive plasma start-up experiments on the TST-2 spherical tokamak using waves in the lower-hybrid frequency range. *Nuclear Fusion*, 55(7):073003, 2015.
- [16] T. Shinya, Y. Takase, S. Yajima, C. Moeller, H. Yamazaki, N. Tsujii, Y. Yoshida, A. Ejiri, H. Togashi, K. Toida, et al. Plasma current start-up experiments using outboard-and top-launch lower hybrid wave on the TST-2 spherical tokamak. *Nuclear Fusion*, 57(3):036006, 2016.
- [17] A. Smirnov, R. Harvey, and K. Kupfer. A general ray tracing code GENRAY. *Bull Amer. Phys. Soc*, 39(7):1626, 1994.
- [18] Y. Takase, A. Ejiri, H. Kakuda, Y. Nagashima, T. Wakatsuki, O. Watanabe, P. Bonoli, O. Meneghini, S. Shiraiwa, J. Wright, et al. Development of a plasma current ramp-up technique for spherical tokamaks by the lower hybrid wave. *Nuclear Fusion*, 51(6):063017, 2011.
- [19] Y. Takase, A. Ejiri, N. Kasuya, T. Mashiko, S. Shiraiwa, L. Tozawa, T. Akiduki, H. Kasahara, Y. Nagashima, H. Nozato, et al. Initial results from the TST-2 spherical tokamak. *Nuclear fusion*, 41(11):1543, 2001.
- [20] Y. Takase, T. Fukuda, X. Gao, M. Gryaznevich, S. Ide, S. Itoh, Y. Kamada, T. Maekawa, O. Mitarai, Y. Miura, et al. Plasma current start-up, ramp-up, and achievement of advanced tokamak plasmas without

the use of ohmic heating solenoid in JT-60U. *Journal of Plasma and Fusion Research*, 78(8):719–721, 2002.

- [21] Y. Todo, H. Berk, and B. Breizman. Nonlinear magnetohydrodynamic effects on Alfvén eigenmode evolution and zonal flow generation. *Nuclear Fusion*, 50(8):084016, 2010.
- [22] Y. Todo and T. Sato. Linear and nonlinear particle-magnetohydrodynamic simulations of the toroidal Alfvén eigenmode. *Physics of Plasmas (1994-present)*, 5(5):1321–1327, 1998.
- [23] Y. Todo, M. Van Zeeland, and W. Heidbrink. Fast ion profile stiffness due to the resonance overlap of multiple Alfvén eigenmodes. *Nuclear Fusion*, 56(11):112008, 2016.
- [24] H. Togashi, A. Ejiri, H. Homma, T. Shinya, Y. Takase, K. Toida, N. Tsujii, T. Yamaguchi, Y. Yoshida, H. Furui, et al. Thomson scattering measurements in low-density plasmas in the TST-2 spherical tokamak. *Journal of Instrumentation*, 10(12):C12020, 2015.
- [25] S. Tsuda, A. Ejiri, H. Tanaka, Y. Takase, M. Uchida, T. Maekawa, N. Tsujii, and T. Takeuchi. Measurement of ion temperature and flow in RF start-up plasmas in TST-2 and LATE. *Plasma and Fusion Research*, 10:1202064–1202064, 2015.
- [26] N. Tsujii, Y. Takase, A. Ejiri, T. Shinya, H. Togashi, S. Yajima, H. Yamazaki, C. Moeller, B. Roidl, M. Sonehara, et al. Numerical modeling of lower hybrid current drive in fully non-inductive plasma start-up experiments on tst-2. *Nuclear Fusion*, 57(12):126032, 2017.
- [27] M. Ushigome, S. Ide, S. Itoh, E. Jotaki, O. Mitarai, S. Shiraiwa, T. Suzuki, Y. Takase, S. Tanaka, T. Fujita, et al. Development of completely solenoidless tokamak operation in JT-60U. *Nuclear fusion*, 46(2):207, 2006.
- [28] T. Wakatsuki, A. Ejiri, T. Shinya, Y. Takase, H. Furui, J. Hiratsuka, K. Imamura, T. Inada, H. Kakuda, H. Kasahara, et al. Plasma current start-up experiments using a dielectric-loaded waveguide array antenna in the TST-2 spherical tokamak. *Nuclear Fusion*, 54(9):093014, 2014.

- [29] H. Wang and Y. Todo. Linear properties of energetic particle driven geodesic acoustic mode. *Physics of Plasmas (1994-present)*, 20(1):012506, 2013.
- [30] J. C. Wright, P. T. Bonoli, A. E. Schmidt, C. K. Phillips, E. J. Valeo, R. W. Harvey, and M. A. Brambilla. An assessment of full wave effects on the propagation and absorption of lower hybrid waves. *Physics of Plasmas*, 16(7), 2009.